JGR Space Physics

RESEARCH ARTICLE
10.1029/2019JA027745

Direct Observations of a Polar Cap Patch Formation Associated With Dayside Reconnection Driven Fast Flow

Jiaen Ren[1], Shasha Zou[1], Elizabeth Kendall[2], Anthea Coster[3], Kevin Sterne[4], and Michael Ruohoniemi[4]

[1]Climate and Space Sciences and Engineering Department, University of Michigan, Ann Arbor, MI, USA, [2]SRI International, Menlo Park, California, USA, [3]Haystack Observatory, Massachusetts Institute of Technology, Westford, MA, USA, [4]SuperDARN HF Radar Group, Virginia Tech, Blacksburg, VA, USA

Key Points:
- Formation of a polar cap patch was directly observed by the GPS TEC maps and Sondrestrom ISR
- Dayside magnetic reconnection-driven fast flow near cusp carrying low-density cold plasma segmented the SED plume into polar cap patches
- The *F* layer height within SED before it enters the cusp is important in determining the most efficient segmentation mechanism

Supporting Information:
- Supporting Information S1

Correspondence to:
J. Ren,
jiaenren@umich.edu

Citation:
Ren, J., Zou, S., Kendall, E., Coster, A., Sterne, K., & Ruohoniemi, M. (2020). Direct observations of a polar cap patch formation associated with dayside reconnection driven fast flow. *Journal of Geophysical Research: Space Physics*, *124*,e2019JA027745. https://doi.org/10.1029/2019JA027745

Received 18 DEC 2019
Accepted 6 MAR 2020
Accepted article online 25 MAR 2020

Abstract Dayside solar-produced concentrated *F* region plasma can be transported from the midlatitude region into the polar cap during geomagnetically disturbed period, creating plasma density irregularities like polar cap patches, which can cause scintillation and degrade performance of satellite communication and navigation at polar latitudes. In this paper, we observed and investigated a dynamic formation process of a polar cap patch during the 13 October 2016 intense geomagnetic storm. During the storm main phase, storm-enhanced density (SED) was formed within an extended period of strong southward interplanetary magnetic field (IMF) B_z condition. Total electron content (TEC) map shows that a polar cap patch was segmented from the SED plume. The Sondrestrom Incoherent Scatter Radar (ISR) was right underneath the segmentation region and captured the dynamic process. It shows that the patch segmentation was related with a sudden northeastward flow enhancement reaching ~2 km/s near the dayside cusp inflow region. The flow surge was observed along with abrupt *E* region electron temperature increase, *F* region ion temperature increase, and density decrease. The upstream solar wind and IMF observations suggest that the flow enhancement was associated with dayside magnetic reconnection triggered by a sudden and short period of IMF B_y negative excursion. Quantitative estimation suggests that plasma density loss due to enhanced frictional heating was insufficient for the patch segmentation because the elevated *F* region density peaking at ~500 km made dissociative recombination inefficient. Instead, the patch was segmented from the SED by low-density plasma transported by the fast flow channel from earlier local time.

1. Introduction

High-latitude ionosphere is characterized by low-density *F* region plasma as compared with the midlatitude sunlit region due to higher solar zenith angle and thus lower extreme ultraviolet (EUV) ionizations. During geomagnetically disturbed periods, however, high-density thermal plasma on the dayside can be transported poleward into the polar cap by enhanced and equatorward-expanding high-latitude electric fields. Consequently, structures of dense *F* region plasma can be present in the polar cap usually with large density gradients and therefore irregularities, which can cause disturbances and scintillations on navigation and satellite communication signals in the polar region.

During a geomagnetic storm, a ridge of significantly increased *F* region plasma density often forms near noon and postnoon magnetic local times (MLTs) at subauroral latitudes, which is termed as storm-enhanced density (SED) (Foster, 1993). Under the effect of high-latitude convection flow, the dense plasma can extend northwestward toward the dayside cusp near noon and form a plume-like structure. The main contribution to the density increase within the SED is the imbalanced production and loss. That is, the plasma is lifted to higher altitudes with lower recombination rate while solar EUV production is still ongoing in the sunlit region. The lifting can be caused by the vertical component of poleward $E \times B$ drifts, as a result of eastward penetrating electric fields at subauroral and midlatitude regions (David et al., 2011; Deng & Ridley, 2006; Heelis et al., 2009; Zou et al., 2013, 2014; Zou & Ridley, 2016). Another important factor that affects plasma vertical motions is thermospheric wind. During storm period, enhanced auroral activities and heating can lead to net equatorward winds at subauroral latitudes, which would push plasma upward along the magnetic field lines (Lu et al., 2012). The dynamic evolution of SED

is determined by the interplay between the electric fields and thermospheric winds (Zou et al., 2014). A more recent modeling study by Liu et al. (2016) shows that while the E × B drift is the dominant factor in generating the SED at topside ionosphere, thermospheric wind plays a more important role in SED formation for low *F* region ionosphere.

As the SED plume reaches the dayside cusp, the high-density plasma within the plume can be entrained into convection inflow region and then enter the polar cap during periods of southward IMF (e.g., Thomas et al., 2013). A sustained transport of such dense plasma can form a large-scale transpolar structure from dayside to nightside known as the tongue of ionization (TOI) (Foster et al., 2005; Knudsen, 1974; Moen et al., 2008; Sato & Rourke, 1964; Zhang et al., 2015). Hosokawa et al. (2010) reported all-sky imager observations of a TOI during a storm on 14–16 December 2006, which showed its dynamic motion and mesoscale structures. Based on measurements from the SuperDARN radars, they suggested that while the absence of large-scale convection pattern changes during periods of stable IMF allows a continuous structure of the TOI, small-scale flow channels near the cusp, probably associated with the dayside transient magnetic reconnection, can be responsible for those mesoscale patterns within the TOI. By combining vertical total electron content (TEC) maps derived from the Global Positioning System (GPS) data and Super Dual Auroral Radar Network (SuperDARN) convection pattern, Thomas et al. (2013) demonstrated formation of a TOI from a SED plume under the effect of equatorward extending convection electric fields during a storm on 26–27 September 2011. They also observed enhanced HF backscatters associated with small-scale field-aligned irregularities within the TOI but not within the SED region, indicating that those small-scale structures are caused by modulations of electric fields near the dayside polar cap boundary.

During periods of unsteady IMF B_y and B_z, the convection pattern near the dayside cusp can change very dynamically. As a result, as the SED plume is entrained into the convection flows, the large-scale plasma plume can break into smaller-scale patches, which are known as polar cap patches. By definition, polar cap patches are islands (~100–1,000 km in scale size) of high-density ionospheric *F* region plasma with low-density surrounding regions (Crowley, 1996; Weber et al., 1984).

The creation of polar cap patches requires a source of high-density plasma and a mechanism to cut the large-scale plasma source into patches. While a good understanding of the sources has been obtained, the cutting mechanisms still remain controversial. As for the sources, dayside midlatitude solar EUV-produced plasma and SED during storm times are generally believed to be the major reservoir for polar cap patches (e.g., Ren et al., 2018). In addition, soft particle precipitation can also become a potential source (Oksavik et al., 2006; Walker et al., 1999) but produce relatively weaker patches.

Besides the source, a mechanism to separate a portion of high-density plasma from the reservoir, for example, the SED plume, is needed to produce patches. Several mechanisms have been proposed: temporal variation of the size of the ionospheric convection pattern (Anderson et al., 1988), transient dayside magnetic reconnection (Lockwood & Carlson, 1992), plasma fast flow channels causing enhanced recombination and low-density regions (Valladares et al., 1994, 1996), and IMF B_y reversals and cusp particle precipitation (Rodger et al., 1994). Using numerical simulations, a more recent study by Wang et al. (2019) shows that intensified Birkeland Current Boundary Flows (BCBF) associated with enhanced westward drifting partial ring current can cut the SED into patches through increased frictional heating and recombination, without requirements for IMF shifts or dayside reconnections. In recent years, the development of observational instruments provides great opportunities to put the proposed mechanisms to test.

Understanding the formation of these high-latitude density structures is of significant practical importance. Studies have shown that the irregularity structure sizes within these patches can vary from hundreds of kilometers to tens of meters (Carlson, 2012), possibly due to gradient drift instability (e.g., Tsunoda, 1988); thus, they may disrupt transionospheric radio waves varying from military and governmental high frequency (HF) communication to satellite ultra-high frequency (UHF) communication and Global Navigation Satellite Systems (GNSS). Severe communication outages can be caused (Basu et al., 1987, 1988) by patches with density higher than 10^6 cm^{-3} between the line of sight (LOS) of the satellite and the receiver. The associated amplitude and phase scintillations may cause increased uncertainty or even loss of lock of GNSS receivers.

In this paper, we investigated the dynamic transport and multiscale plasma density structures of high-latitude ionosphere during a geomagnetic storm on 13 October 2016, based on vertical GPS TEC maps, Active Magnetosphere and Planetary Electrodynamics Response Experiment (AMPERE) field-aligned currents (FACs) maps, SuperDARN convection patterns, and Sondrestrom ISR. In section 2, we give a brief introduction to the instruments and data sets that were used in the study. Section 3.1 outlines the geomagnetic storm event on 13 October 2016. Section 3.2 shows ionosphere plasma density increase in midlatitude and subauroral regions and discusses how the dense plasma was transported into the polar cap during the storm main phase. Section 3.3 focuses on the formation of a polar cap patch during the event by carefully examining conjunction observations from the GPS TEC, SuperDARN convection, and Sondrestrom ISR. Finally, section 4 summarizes the observations and conclusions.

2. Instrumentation and Data

2.1. GPS Total Electron Content

In this study, GPS TEC data are used to show large-scale plasma structures and their transport from midlatitude to high-latitude ionosphere. The GPS TEC data were obtained from the Madrigal database, and the detailed data processing method can be found in Rideout and Coster (2006) and Vierinen et al. (2016). The conversion from the LOS TEC values to vertical TEC is done by assuming a slab ionosphere at 350 km altitude, and only data points with elevation angle above 30° have been used. The TEC data shown in this paper have a temporal resolution of 5 min and spatial resolution of 1° × 1° in latitude and longitude with a 3° × 3° median filer applied to overcome the sparsity of data in the polar cap.

2.2. Super Dual Auroral Radar Network

We used the SuperDARN convection maps to see how the transport of ionosphere density structures is affected by the large-scale convection pattern during the storm period. As an international network of more than 30 HF radars, SuperDARN covers areas from midlatitudes to the polar regions for both hemispheres. The low-power HF radars operate continuously and measure the velocity of field-aligned plasma irregularities projected in the LOS of radar beams. The two-dimensional E × B velocity vectors can be derived when they are measured within the common field of view by two radars. A solution of high-latitude electrostatic potential field can be determined by combining all the velocity measurements and model results for areas where no observational data are available (Ruohoniemi & Baker, 1998). As a result, SuperDARN provides large-scale ionospheric convection maps on equal-area grids (100 km × 100 km) in the Altitude Adjusted Corrected Geomagnetic (AACGM) coordinate (Shepherd, 2014) for every 2 min.

2.3. Active Magnetosphere and Planetary Electrodynamics Response Experiment

AMPERE FACs maps are used to indicate the location of the auroral oval and polar cap boundary and show expansions or contractions of the polar cap. Based on measurements of the magnetic field perturbations from the Iridium Communications constellation of more than 70 satellites at low Earth orbits (~780 km), AMPERE provides a global view of FACs. The orbits of satellites form 12 longitudinal planes equally spaced by 2 hr, and satellites along each track are separated by 9 minutes. The magnetic field perturbation data are calibrated and then used in spherical harmonic inversion (Green et al., 2006; Waters et al., 2001). The FACs are derived by taking the curl of the fitted perturbations and are provided in the AACGM coordinates on 1 hr MLT by 1° magnetic latitude (MLat) grids for every 2 min. More detailed descriptions of the data product can be found in Anderson et al. (2014) and references therein.

2.4. Sondrestrom ISR

The ISRs are powerful ground-based instruments for ionosphere observations. By measuring the backscattered signals from electrons in the ionosphere, the ISRs have the ability to resolve the altitudinal profiles of electron density, electron and ion temperatures, and LOS ion velocity simultaneously. During this event, the Sondrestrom radar observed a fast flow channel associated with dayside reconnection when it was located near the dayside cusp, and in section 3.3, we will discuss the contribution of this fast flow channel to the formation of a polar cap patch. The Sondrestrom radar (67°N, 309°E, geographic; 74°N geomagnetic) was located near the west coast of Greenland and was operating under composite scans mode during this event. Under this mode, the radar was alternating between two scanning planes both roughly parallel to the magnetic meridian with one tilted slightly westward and the other tilted slightly eastward. Each scan

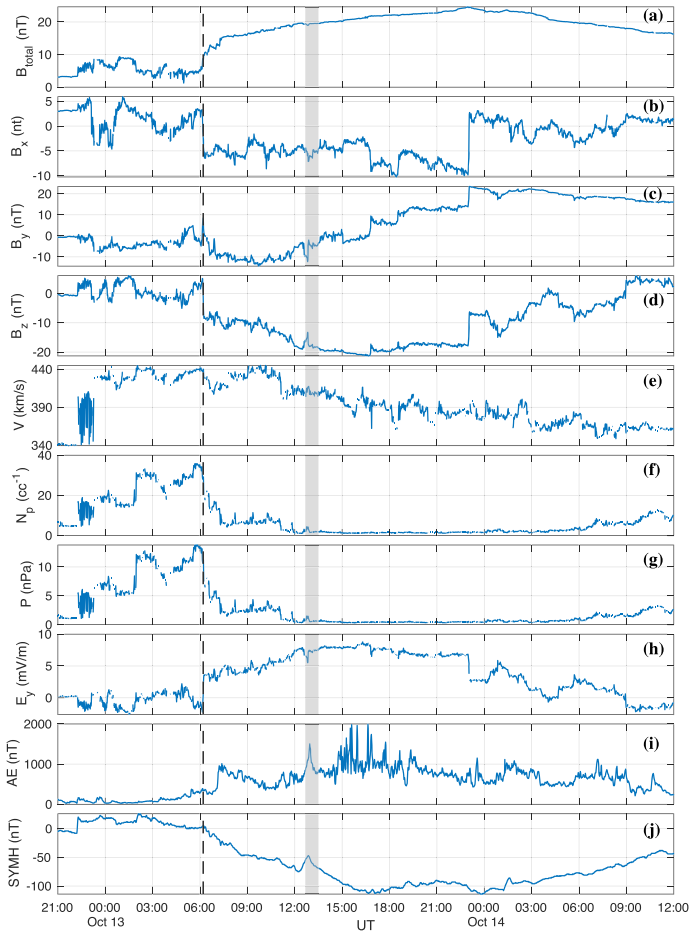

Figure 1. Solar wind and IMF conditions, provisional AE index and SYM-H component from 12 UT on 12 October to 21 UT on 14 October 2016, obtained from the NASA OMNI database. The geomagnetic storm is initiated at the arrival of an interplanetary shock and then enters the main phase as the solar wind presents a clear magnetic cloud structure. The shaded area marks the period when the generation of the polar cap patch was observed in TEC maps.

takes ~4 min and consists of 14 beams directions (Figure 6) with measurement ranges from ~120 to ~1,300 km, and the altitude resolution changes from ~23 km in the *E* region to ~65 km in the *F* region. By pairing the corresponding LOS velocity measurements at the same latitude and altitude from two successive scans (one eastward and one westward), an average *F* region two-dimensional horizontal velocity can be resolved for a given latitude. Finally, the resolved velocities are averaged in 0.25° latitude bins covering up from ~65° to ~80° MLat. In this study, for plasma density and temperatures, the latitude scans at a certain altitude were obtained by selecting the measurement at the closest altitude from each beam within a scan. In addition, data points of the resolved velocities with uncertainties larger than 250 m/s were dropped.

3. Observations

3.1. Solar Wind and IMF Condition for the 12–14 October 2016 Storm

Figure 1 shows the IMF (a–d) and solar wind (e–g) conditions, interplanetary electric field (h), AE (i), and SYM-H (j) indices from 12 UT on 12 October to 21 UT on 14 October 2016. The IMF and solar wind parameters were obtained from the NASA OMNI database, and they were observed by the WIND spacecraft and then time-shifted to the Earth's bow shock nose. This geomagnetic storm was a classic interplanetary coronal mass injection (ICME)-driven intense storm with clear shock, sheath, and magnetic cloud signatures. The storm was initiated with a storm sudden commencement (SSC) at 22:16 UT on 12 October,

induced by the sudden enhancement of the solar wind dynamic pressure when the interplanetary shock in front of the ICME arrived. The solar wind speed jumped from ~340 to ~440 km/s (Figure 1e) at the shock and then decreased gradually. Typical ICME magnetic cloud signatures, including strong magnetic field, slow magnetic field rotation, low proton number density, and plasma thermal pressure, can be seen throughout an extended period of ~34 hr starting from 06:12 UT on 13 October and ending at ~06 UT on 14 October. The magnetic cloud started with a sudden southward turning of the IMF B_z from +5 to −9 nT at 06:12 UT (dashed line in Figure 1), which kept decreasing since then and reached −21 nT at 16:41 UT on 13 October. During the same period, the IMF B_y started with negative values as large as −14 nT and then gradually turned to positive and reached +23 nT at 23:02 UT on 13 October. The extended period of strong southward IMF B_z caused an intense geomagnetic storm with the minimum SYM-H index reaching −113 nT and AE peaking at ~2,000 nT.

3.2. General Ionosphere Responses to this Storm

Figure 2 shows GPS TEC maps (left) and AMPERE FAC maps (right) with high-latitude ionosphere convection contours from SuperDARN at five selected time cadences. These five times were right before (2a) and after (2b) the IMF B_z southward turning at 06:12 UT, 1.5 and 2.5 hr (2c and 2d) after the southward turning, and near the SYM-H minimum (2e) at 18:37 UT.

Figure 3 shows the time series plot of the IMF B_y and B_z (3a), reproduced for convenience, and average MLat of dayside (11–13 MLT) polar cap boundary (3b), which is approximated by location of the peak Region 1 currents estimated from AMPERE FAC measurements, similar to the method used in Clausen et al. (2013). Additionally, in Figure 3c, a keogram of the averaged GPS TEC near magnetic noon (11–13 MLT) is shown from 21 UT on 12 October to 12 UT on 14 October 2016.

From Figures 2a and 2b, it can be seen that the size of the convection pattern had expanded significantly at 06:14 UT comparing with that at 06:10 UT, as a result of the sudden southward turning of the IMF B_z occurring at 06:12 UT, as indicated by the vertical dashed line in Figure 3. About 1.5 hr later, as shown in Figures 2c, 2d, and 3c, the dayside midlatitude ionosphere around noon showed significant plasma density enhancement from 07:52 to 08:52 UT, indicating a positive ionosphere storm occurred during this period. In Figures 2d and 3c, at 08:52 UT, a sharp TEC boundary with latitudinal density gradient as large as −1.8 TECU/degree can be seen at ~65° MLat and ~12 MLT, well aligned with the outermost contour of the fitted SuperDARN convection pattern and the Region 2 downward FACs. As the IMF B_z kept decreasing after 08:52 UT, the polar cap open-closed field line boundary and the convection pattern keep expanding further equatorward, as indicated in Figure 3b, and the sharp TEC boundary also moved equatorward accordingly. Starting from ~11 UT in Figure 3c, midlatitude plasma with TEC of ~12 TECU was transported poleward into the polar cap near noon from the sharp TEC boundary. The transport had been intermittent from ~11 to ~16 UT, and several polar cap patches were observed to form and enter the polar cap during this time period. After ~16 UT, as the southward IMF B_z approached its maximum and the polar cap boundary reached as low as ~62° MLat, more continuous and larger-scale poleward transport of subauroral high-density plasma (~20 TECU) was present until ~20:30 UT.

During this period, while a large-scale TOI structure of high-density plasma was present on the TEC map, as shown in Figure 2e at 18:36 UT, from the TEC keogram in Figure 3c, we can see density variations of smaller scales were embedded within this large-scale density structure. When the TOI was present during ~15 to ~18 UT, the sharp TEC boundary rapidly moved to lower latitudes from ~50° to ~40° MLat. After ~21 UT, as the high-density source region remained below ~40° MLat and the polar cap boundary started to retreat poleward, the plasma density dropped to a level even lower than it was at same UT but 24 hr earlier before the geomagnetic storm occured, as can be seen from Figure 3c, forming a deep midlatitude trough.

In Figure 3c we have seen that after the sudden southward turning of the IMF B_z, the polar cap started to expand to lower latitudes, and about 1.5 hr later, a positive ionosphere storm occurred, significantly increasing the subauroral plasma density. During ~11 to ~16 UT, however, the poleward transport of the plasma was intermittent and, as a result, several polar cap patches instead of a relatively uniform TOI were formed during this time period. From the SuperDARN convection pattern in Figure 2d, we can see that the convection inflow region during this period was shifted toward dawn side at around 10 MLT due to the negative

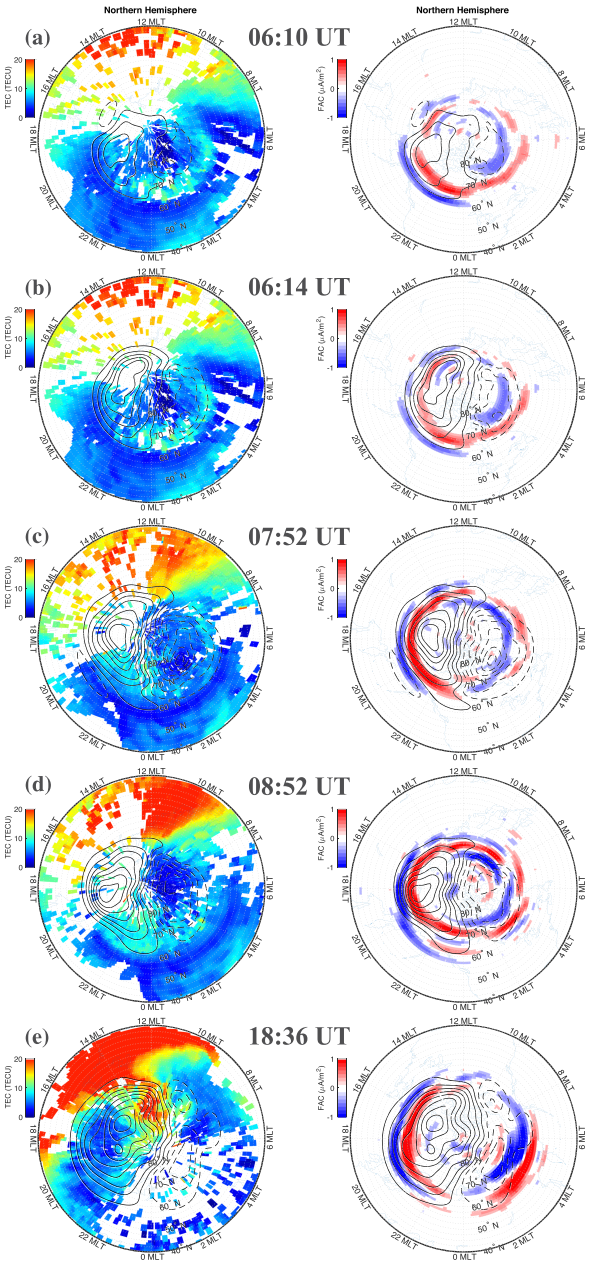

Figure 2. GPS TEC maps from the Madrigal database (left) and AMPERE FACs maps (right) with high-latitude ionosphere convection pattern from SuperDARN overlaid at (a) 06:10 UT, (b) 06:14 UT, (c) 07:52 UT, (d) 08:52 UT, and (e) 18:36 UT. The outermost dashed (solid) contour of the convection cell corresponds to 3 kV (−3 kV) equipotential line, and the interval between two contours is 6 kV. The size of the convection pattern had expanded significantly at 06:14 UT comparing with that at 06:10 UT, as a result of the sudden southward turning of the IMF B_z occurring at 06:12 UT. Dayside midlatitude ionosphere around noon showed significant plasma density enhancement from 07:52 to 08:52 UT as an ionosphere storm entered the positive phase. Magnitude of the FACs system also increased comparing (c) and (d) with (a) and (b).

IMF B_y condition, while the subauroral density enhancement was mainly located on the noon and postnoon MLTs. A sharp TEC boundary instead of a TOI was formed because the convection direction at the boundary near the high-density source region was mostly westward instead of poleward. It was not until ~16 UT when the IMF B_y started to turn into positive that the inflow region shifted to where the enhanced density was and formed a large-scale TOI structure.

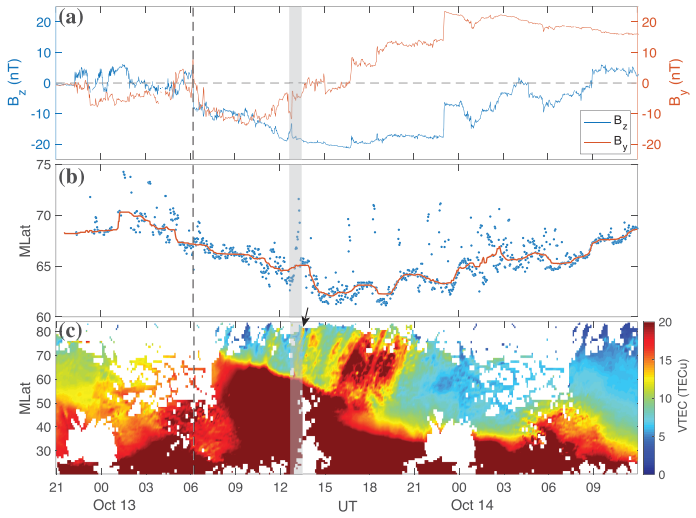

Figure 3. (a) IMF B_y and B_z from the NASA OMNI database. (b) The blue dots show estimate Region 1 FACs average latitude between 11 and 13 MLT for every 2 min, as an approximation for the latitudes of polar cap boundary. The red curve is obtained by applying median filter with a 50-point window. (c) GPS TEC keogram between 11 and 13 MLT from the Madrigal database, from 21 UT on 12 October to 12 UT on 14 October 2016. The vertical dashed line marks the onset of a southward IMF B_z turning at 6:12 UT. The shaded area indicates the period of a polar cap patch formation at ~13 UT, as discussed in section 3.3. The arrow marks the trace of the patch in the TEC keogram.

3.3. Polar Cap Patch Formation Near Cusp

In this section, we will show in detail the formation of a polar cap patch. Figure 4 shows a direct observation of formation of polar cap patch in the GPS TEC map as a result of a fast flow appearance in the convection inflow region from 13:00 to 13:15 UT on 13 October 2016 shown in Figure 5.

In Figure 4, ionosphere cusp location can be estimated by identifying the dayside convection inflow region from the SuperDARN convection pattern and between the merging region of the dawn and dusk Region 1 FACs from the AMPERE data. The TEC map in Figure 4a shows that, at 13:00 UT when the dayside cusp was near the magnetic noon, the convection inflow region extended into the high-density plasma source region at ~65° MLat and ~12° MLT. As a result, the poleward convection flow near magnetic noon directly transported the high-density plasma from the source region into the polar cap. At 13:08 UT (4b), a convection flow kink appeared near the magnetic noon as the convection inflow region shifted toward the dawn side, and the boundary of convection pattern slightly retreated to higher latitude, which could also be seen from Figure 3b within the shaded area. The FACs pattern at the same time shows that the kink was near the upward and downward Region 1 FACs overlapping region and thus was the typical cusp location. After this convection flow configuration changed, plasma with lower density was transported to the polar cap, as seen at 13:12 UT in Figure 4c. And as a result, the high-density plasma moving poleward into the polar cap seen in 4a was cut off from its subauroral source region and became a polar cap patch. The flow kink shown in the SuperDARN convection map was derived based on real radar measurements, as shown in Figure S1 in the supporting information.

As shown in Figure 5, this sudden flow direction change near cusp was also observed by the Sondrestrom ISR, which provides us altitudinal profiles and latitude scans of multiple physical parameters. From Figures 4 and 5c, on a large scale, it can be seen that when the radar corotated into the dayside convection inflow region, the background flow direction changed gradually from eastward (blue) to northward (green). However, following a sudden southward IMF B_z decrease (5a, black curve) and further-negative excursion of the IMF B_y (5a, blue curve) from 12:35 to 12:50 UT, a channel of northeastward flow burst exceeding 2000 m/s can be seen at ~13:00 UT (10 MLT) in Figures 5b and 5c, and it was moving poleward. The plasma in the background surrounding region showed dominantly northward motion with velocity of 500–1,000 m/s. Both *E* region electron (5d) and *F* region ion temperatures (5f) showed sudden enhancement associated with the fast flow channel. The *E* region electron temperatures increase indicated presence of energetic

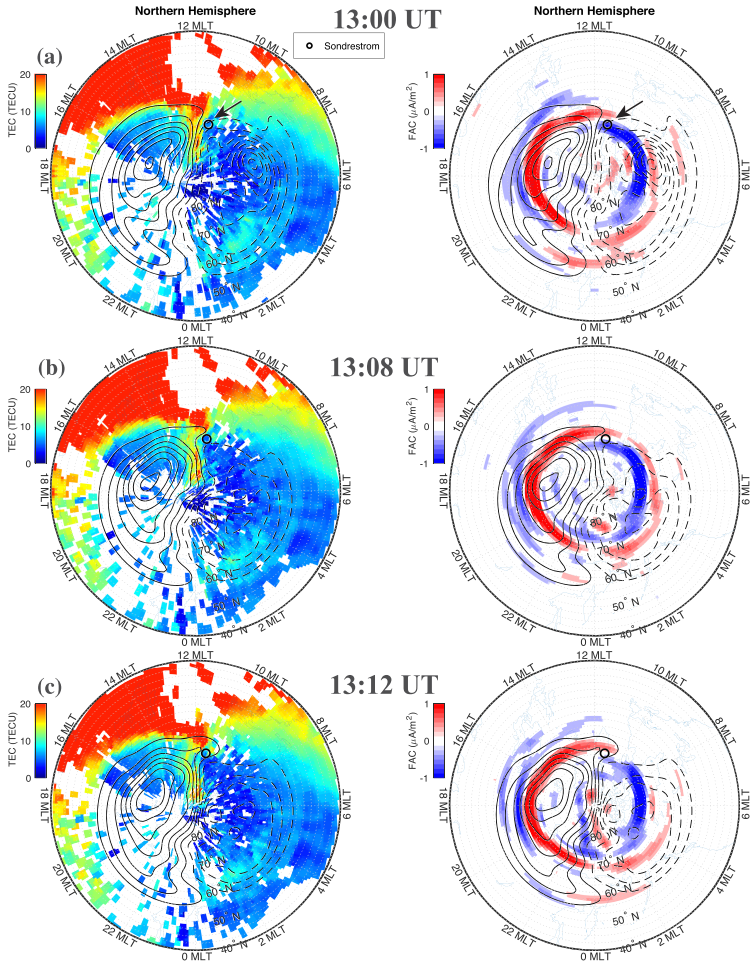

Figure 4. GPS TEC, AMPERE FACs maps, and SuperDARN convection patterns at 13:00 UT (a), 13:08 UT (b), and 13:12 UT (c) on 13 October 2016. The Sondrestrom ISR, marked by the black circle, was located near the dayside convection inflow region around 11 MLT. From the TEC map, it can be seen that high-density plasma moving poleward into the polar cap was segmented into patches due to the sudden convection direction change near the inflow region. SuperDARN had real radar measurements near the convection kink, as shown in Figure S1.

particle precipitation, and the *F* region ions were heated by frictional heating within the fast flow. Meanwhile, as shown in Figures 5e and 5g, a distinct area of low density and cold electron temperature in the *F* region was also observed associated with the fast flow channel.

The observed plasma density decrease could be caused by the fast flow through two possible ways. The first one is the increased recombination rate due to frictional heating within the fast flow. The other one is low-density plasma nearby transported by the flow channel into the radar field of view. In order to determine which factor had played a more dominant role in this case, careful examinations on the measurements from individual radar scans are required.

In Figure 6, the Sondrestrom ISR measurements from three consecutive eastward scans show plasma properties before, during, and after the period that the fast flow appears, respectively. During the first scan from ~12:57 to ~13:01 UT, the radar had seen hot and dense solar EUV-produced plasma with density reaching ~$10^{11.5}$ m^{-3} (Figure 6a) and electron temperature over 2,500 K (6d), throughout the radar field of view from 65° to 80° latitude. The height of peak electron density (hmF2) was lifted up to ~500 km altitude, most likely due to the upward component of the E × B drift as the plasma is moving poleward on the dayside, which can be seen from the radar ion LOS velocity measurements (6j). Within 10 min after the first scan, starting from ~13:07 to ~13:11 UT, a structure of cold plasma with significantly lower density ~10^{10} m^{-3} and electron

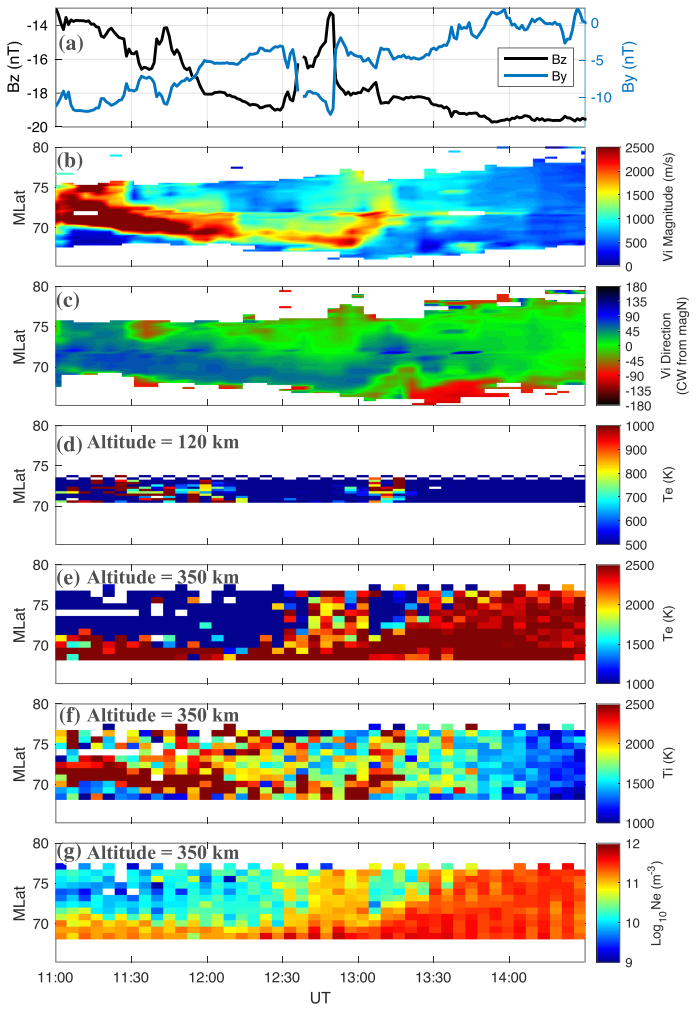

Figure 5. (a) The solar wind IMF B_y and B_z components from the OMNI database. Sondrestrom ISR latitude scans of plasma convection velocity (b) speed and (c) direction (zero starts from the magnetic north and rotates clockwise for positive values), electron temperature at (d) 120 km and (e) 350 km altitude, (f) ion temperature, and (g) electron density at 350 km altitude from 11:00 to 14:30 UT on 13 October 2016. For the Sondrestrom ISR, MLT = UT – 3 hr. A northeastward fast flow channel as strong as 2 km/s could be seen at around 13 UT (10 MLT), and it was moving toward higher latitudes, while the plasma in the background showed northward motion with velocity of 500–1,000 m/s. Electron precipitation at 120 km, ion temperature increase, electron temperature, and density decrease at 350 km were observed along with the fast flow channel.

temperature below 1,000 K appeared in the middle of the radar field of view (6b and 6e). The electron density profiles within the structure peaked at ~250 km altitude. The most upward beam in the middle, which also pointed slightly toward the east as shown in the bottom right panel of Figure 6, had seen strong LOS ion velocity over 1,000 m/s away from the radar (6k), indicating the presence of eastward fast flow overhead. The drastic differences in the plasma density, temperature, and hmF2 were strong evidences indicating that the low-density structure was transported into the radar field of view from a different plasma source than the high-density plasma seen during the first scan, most likely from the polar cap on the dawn side according to TEC maps shown in Figure 4.

In addition, quantitative estimations of the density decrease caused by the frictional heating have been conducted and the results are shown in Figure 7. By averaging the measurements taken from the nine beams above 71.7° MLat in each scan, the altitudinal profiles of ion temperature and electron density were calculated for 12:57 and 13:07 UT, as shown in Figures 7a and 7b, respectively. Besides, the density profiles of neutral N_2 provided by the Madrigal database using the MSIS 2000 model are also shown in Figure 7c, which is

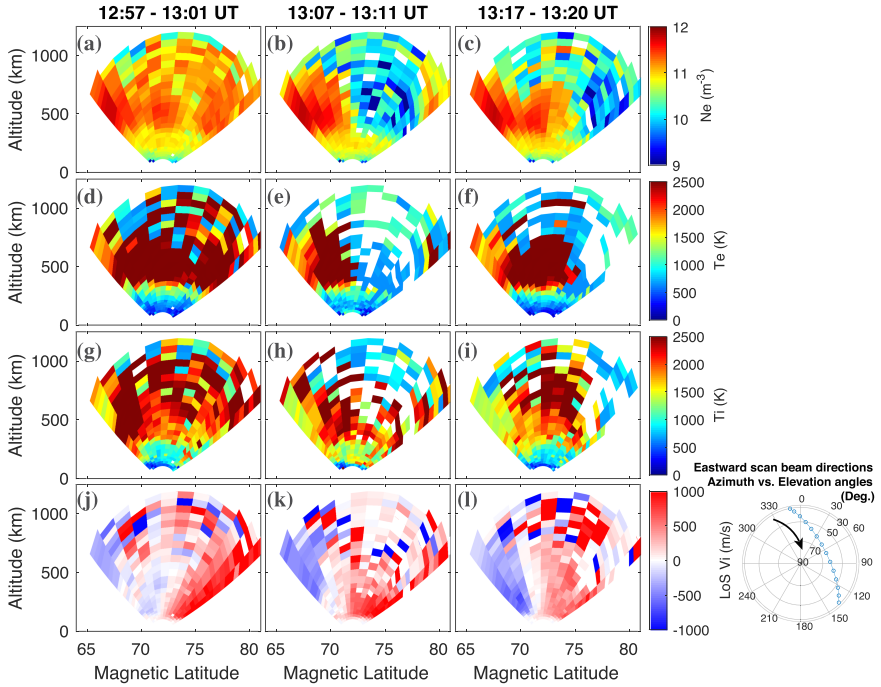

Figure 6. Sondrestrom ISR measurements of (a–c) electron density, (d–f) electron temperature, (g–i) ion temperature, and (j–l) ion LOS velocity (positive values indicate direction away from the radar) from three consecutive eastward scans before, during, and after the density decrease at ~13:10 UT, when the fast flow was observed. The pointing directions of the radar eastward scan (always from the north to the south) is shown at the bottom right panel.

required for the estimation. In Figure 7d, we demonstrated a comparison between the total density decrease measured by the Sondrestrom ISR from 12:57 to 13:07 UT and the estimated density decrease caused by the frictional heating.

Although the enhanced ion flow speed leads to noticeable ion-neutral frictional heating at altitudes below 250 km (Figure 7a), for altitudes above 300 km, the frictional heating was not sufficient to account for the density decreases observed, mainly due to the lack of neutrals above 300 km. At 12:57 UT, according to Figure 5b, the mean plasma flow speed at ~72° MLat was ~1345 m/s, while at 13:07 UT the flow speed rapidly increased to ~2,371 m/s, creating enhanced frictional heating through ion-neutral collisions, which increased the ion temperature within the next 10 min mainly below ~250 km, as can be seen in Figure 7a. Since the neutral density was much higher than the ion density below ~600 km, the time scale for the neutral temperature to increase was much longer, so we can assume that at 13:07 UT, the neutral temperature remained the same as the ion temperature at 12:57 UT. For altitudes between ~200 and ~700 km, the dominant ion species is O^+. Based on the equations given by St.-Maurice and Torr (1978), as a result of the elevated ion temperature and enhanced flow speed, the charge exchange rates between O^+ and N_2 and between O^+ and O_2 could have increased by up to ~250% and ~80%, respectively. Description of the calculations in details can be found in Text S1. Because the dissociative recombination of the resulting NO^+ and $O_2{}^+$ was significantly faster than radiative recombination of O^+, we can estimate the density decrease by computing how much O^+ had been lost by charge exchange within 10 min. As shown in Figure 7d, the frictional heating could only account for the density decrease below ~300 km altitude, while above ~300 km, where the largest density decrease is observed, the contribution from the enhanced frictional heating was several order of magnitudes lower than the observed values. This is mainly because the neutral density, shown in Figure 7c, decreases exponentially with altitude. In additional, considering that the neutrals could also be heated to some extent and lead to N_2 and O_2 density increase as a result of thermosphere expansion, we also did a similar estimation with neutral density doubled, but the results were not affected by much. This estimation suggests that enhanced frictional heating was not the dominant effect that accounts for the appearance of the low-density structure seen above ~300 km and also the low TEC structure seen in the TEC map.

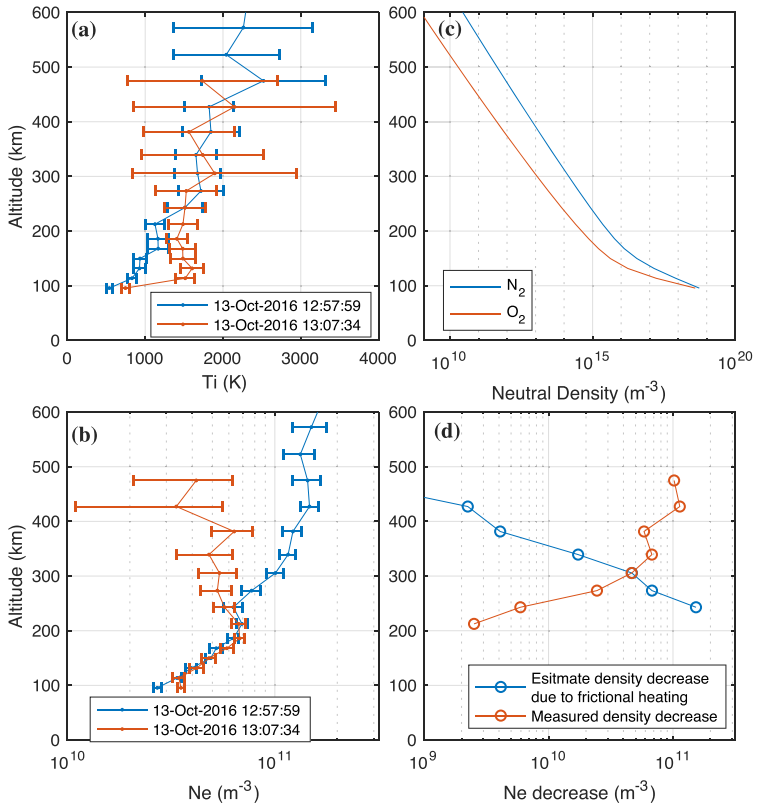

Figure 7. (a and b) Altitude profiles of ion temperature and electron density measured by Sondrestrom ISR eastward scans at 12:57 and 13:07 UT. The altitude profiles were calculated by averaging the measurements from the nine beams above 71.7° MLat in each scan. (c) N_2 density profile provided by Madrigal based on MSIS 2000 model. (d) Estimate plasma density decrease caused by frictional heating using formulations in St.-Maurice and Torr (1978), compared with total density decrease in observation from 12:57 to 13:07 UT, as shown in (b).

According to the analysis above, it can be concluded that the low-density structure observed was transported by the northeastward fast flow channel from a nearby region on the dawnside and the impact of frictional heating was limited to altitudes below ~300 km.

4. Discussion

This result shows an interesting contrast with the scenario demonstrated by Wang et al. (2019), in which the frictional heating-induced density decrease can account for the segmentation of a SED plume. In both cases, low-TEC regions were observed in the TEC map during the segmentation process; however, a key difference that the two-dimentional TEC maps cannot show is that the plasma vertical density profiles in these two events peaked at very different altitudes. As shown in the Figure 4d of Wang et al. (2019), the density profile peaked at ~300 km at ~4×10^{11} m^{-3} when the boundary fast flow between the Regions and 2 FACs was present, while in our case, the observed SED plume had been significantly lifted and the maximum density was found reaching ~1.9×10^{11} m^{-3} at ~500 km at ~12:57 UT. Since the neutral density drops with altitude exponentially, there are over 3 orders of magnitude less neutrals at 500 km for the ions (mostly O^+) to react with than those at 300 km, making the frictional heating a lot less effective in raising the recombination rate and decreasing the plasma density. To show the importance of hmF2 in affecting the density loss due to frictional heating, we hypothetically lowered the density peak from ~500 to ~300 km while keeping other parameters unchanged, and our estimation showed that the frictional heating could cause a ~1.3×10^{11} m^{-3} density decrease within 10 min, ~3 orders of magnitude larger than it did at ~500 km. In conclusion, the fact that the SED plume had been lifted to a much higher altitude (with hmF2 ~500 km) was the main factor that

made frictional heating effect not important for patch segmentation in this case. Using numerical model, Zou and Ridley (2016) found that SED plasma originating from different local time sectors could have different characteristics, such as NmF2 and hmF2, implying different segmentation mechanisms may exist for SED plasma originating from different local times.

Detailed examinations of sequence of the observations suggest the fast flow surge, and the associated plasma characteristics were ionospheric signatures of magnetic reconnection. At first, following the sudden IMF B_y negative excursion from ~12:40 to ~12:50 UT (Figure 5a), an initial *E* region electron temperature increase can be seen at ~12:52 UT near 72° MLat (Figure 5d), which was due to precipitating particles streaming from the reconnection site. At this latitude, the northeastward flow surge exceeding 2 km/s appeared at ~13:00 UT. Then at ~13:04 UT, significant ion temperature increase at ~350 km altitude was observed, due to frictional heating within the fast flow or particle precipitation from the reconnection site. This series of observations matched very well with the expected signatures of magnetic reconnection reported by Carlson et al. (2004). Carlson et al. (2006) showed the first observation of these signatures from the EISCAT Svalbard radar (ESR) and concluded that it validated the Lockwood and Carlson (1992) mechanism, in which reconnection driven convection flow surge transiently injects corotating subauroral high-density plasma into the polar cap. In their study, under a positive IMF B_y condition, a northwestward flow surge carrying subauroral plasma into the polar cap was seen at ~10 MLT, similar to the local time of our case. The northeastward fast flow we observed was consistent with the negative IMF B_y condition. On the contrary, in our case it was the low-density rather than high-density plasma that is carried by the flow surge, being injected toward noon into the middle of a stream of high-density plasma that was previously transported into the polar cap a few minutes before (see Figure 4). Therefore, the transient flow surge in this case only acted as a segmentation mechanism (with little frictional heating effect). Essentially, the physical process here was most likely the same as that described in the Lockwood and Carlson (1992) mechanism but happened in a different ionosphere precondition (mostly plasma density distribution).

To generalize, a similar scenario of polar cap patch formation as the one discussed in this study requires the following: (1) A structure of high-density plasma lifted in altitude is present in the polar cap near the cusp, which could be either a small-scale stream of plasma that just entered the polar cap from the SED, or a preexisted large-scale TOI; (2) a reservoir of low-density plasma in adjacent regions, such as non-SED high-latitude plasma or the main polar cap trough; and (3) a fast flow channel (most likely driven by dayside reconnection) from the low-density reservoir to the high-density structure. While for those lifted density structures (hmF2 ~500 km), both the low-density reservoir and flow channel are required; for those density structures without being lifted (hmF2 ~300 km), the fast flow channel alone can create segmentation via frictional heating.

5. Summary and Conclusions

In this paper, we investigated the dynamic structuring of high-density plasma from a dayside subauroral SED to the polar cap during a geomagnetic storm on 13 October 2016, based on observations from the GPS TEC maps, AMPERE FACs maps, SuperDARN convection patterns, and Sondrestrom ISR. During the storm main phase, a sudden southward turning of the IMF B_z triggered expansion of the polar cap and a positive ionosphere storm, which created a strong convection pattern and significantly increased the subauroral plasma density as the SED at postnoon MLTs. However, the dayside convection inflow region was shifted toward the dawnside at around 10 MLT due to the negative IMF B_y condition, unfavorable for continuous transport of the SED plasma into the polar cap and formation of TOI. Instead, a dayside magnetic reconnection-driven fast flow channel, triggered by a sudden and short period of IMF B_y negative excursion, transported low-density cold plasma from earlier local time into the convection inflow region and segmented a group of SED plasma into a polar cap patch. Quantitative estimations of the effect of enhanced frictional heating due to the fast flow have been conducted. However, while increased ion temperature was present within the fast flow, it was not sufficient to deplete the SED plasma down to observed values above 300 km, mainly because the *F* region peak in the SED structure had been lifted to altitudes ~500 km, where the neutrals were lacking, and thus, the loss due to the enhanced dissociative recombination was not efficient to deplete the SED plasma.

Acknowledgments

This work is supported by the National Science Foundation NSF1400998. The authors acknowledge the use of SuperDARN data (http://vt.superdarn.org/tiki-index.php). SuperDARN is a collection of radars funded by national scientific funding agencies of Australia, Canada, China, France, Italy, Japan, Norway, South Africa, United Kingdom, and the United States of America. The authors thank the AMPERE team and the AMPERE Science Center for providing the Iridium-derived data products (http://ampere.jhuapl.edu/index.html). The authors also acknowledge the MIT Haystack Observatory for providing the GPS TEC data. The Sondrestrom ISR was operated by SRI International in Menlo Park, California, under the auspices of the U.S National Science Foundation. The GPS TEC data and the Sondrestrom ISR data are available at the CEDAR Madrigal database (http://cedar.openmadrigal.org/). The solar wind IMF data are available at the NASA OMNI database (https://omniweb.gsfc.nasa.gov/ow_min.html).

References

Anderson, B. J., Korth, H., Waters, C. L., Green, D. L., Merkin, V. G., Barnes, R. J., & Dyrud, L. P. (2014). Development of large-scale Birkeland currents determined from the Active Magnetosphere and Planetary Electrodynamics Response Experiment. *Geophysical Research Letters*, *41*, 3017–3025. https://doi.org/10.1002/2014GL059941

Anderson, D. N., Buchau, J., & Heelis, R. A. (1988). Origin of density enhancements in the winter polar cap ionosphere. *Radio Science*, *23*(4), 513–519. https://doi.org/10.1029/RS023i004p00513

Basu, S., MacKenzie, E., & Basu, S. (1988). Ionospheric constraints on VHF/UHF communications links during solar maximum and minimum periods. *Radio Science*, *23*(3), 363–378. https://doi.org/10.1029/RS023i003p00363

Basu, S., MacKenzie, E., Costa, E., Fougere, P., Carlson, H., & Whitney, H. (1987). 250 MHz/GHz scintillation parameters in the equatorial, polar, and auroral environments. *IEEE Journal on Selected Areas in Communications*, *5*(2), 102–115. https://doi.org/10.1109/JSAC.1987.1146533

Carlson, H. C. (2012). Sharpening our thinking about polar cap ionospheric patch morphology, research, and mitigation techniques. *Radio Science*, *47*(4). https://doi.org/10.1029/2011RS004946

Carlson, H. C., Moen, J., Oksavik, K., Nielsen, C., McCrea, I. W., Pedersen, T., & Gallop, P. (2006). Direct observations of injection events of subauroral plasma into the polar cap. *Geophysical Research Letters*, *33*, L05103. https://doi.org/10.1029/2005GL025230

Carlson, H. C., Oksavik, K., Moen, J., & Pedersen, T. (2004). Ionospheric patch formation: Direct measurements of the origin of a polar cap patch. *Geophysical Research Letters*, *31*, L08806. https://doi.org/10.1029/2003GL018166

Clausen, L. B. N., Baker, H., Ruohoniemi, J. B., Milan, J. M., Coxon, S. E., Wing, J. C., et al. (2013). Temporal and spatial dynamics of the regions 1 and 2 Birkeland currents during substorms. *Journal of Geophysical Research: Space Physics*, *118*(6), 3007–3016. https://doi.org/10.1002/jgra.50288

Crowley, G. (1996). Critical review of ionospheric patches and blobs. *Review of Radio Science*, *1993–1996*, 619–648.

David, M., Sojka, J. J., Schunk, R. W., Liemohn, M. W., & Coster, A. J. (2011). Dayside midlatitude ionospheric response to storm time electric fields: A case study for 7 September 2002. *Journal of Geophysical Research: Space Physics*, *116*(A12). https://doi.org/10.1029/2011ja016988

Deng, Y., & Ridley, A. J. (2006). Role of vertical ion convection in the high-latitude ionospheric plasma distribution. *Journal of Geophysical Research*, *111*, A09314. https://doi.org/10.1029/2006JA011637

Foster, J. C. (1993). Storm time plasma transport at middle and high latitudes. *Journal of Geophysical Research: Space Physics*, *98*(A2), 1675–1689. https://doi.org/10.1029/92JA02032

Foster, J. C., Coster, A. J., Erickson, P. J., Holt, J. M., Lind, F. D., Rideout, W., et al. (2005). Multiradar observations of the polar tongue of ionization. *Journal of Geophysical Research*, *110*, A09S31. https://doi.org/10.1029/2004JA010928

Green, D. L., Waters, C. L., Anderson, B. J., Korth, H., & Barnes, R. J. (2006). Comparison of large-scale Birkeland currents determined from Iridium and SuperDARN data. *Annales Geophysicae*, *24*(3), 941–959. hal-00318005f

Heelis, R. A., Sojka, J. J., David, M., & Schunk, R. W. (2009). Storm time density enhancements in the middle-latitude dayside ionosphere. *Journal of Geophysical Research*, *114*, A03315. https://doi.org/10.1029/2008JA013690

Hosokawa, K., Tsugawa, T., Shiokawa, K., Otsuka, Y., Nishitani, N., Ogawa, T., & Hairston, M. R. (2010). Dynamic temporal evolution of polar cap tongue of ionization during magnetic storm. *Journal of Geophysical Research*, *115*, A12333. https://doi.org/10.1029/2010JA015848

Knudsen, W. C. (1974). Magnetospheric convection and the high-latitude F_2 ionosphere. *Journal of Geophysical Research*, *79*(7), 1046–1055. https://doi.org/10.1029/JA079i007p01046

Liu, J., Wang, W., Burns, A., Solomon, S. C., Zhang, S., Zhang, Y., & Huang, C. (2016). Relative importance of horizontal and vertical transports to the formation of ionospheric storm-enhanced density and polar tongue of ionization. *Journal of Geophysical Research: Space Physics*, *121*, 8121–8133. https://doi.org/10.1002/2016JA022882

Lockwood, M., & Carlson, H. C. (1992). Production of polar cap electron density patches by transient magnetopause reconnection. *Geophysical Research Letters*, *19*(17), 1731–1734. https://doi.org/10.1029/92GL01993

Lu, G., Goncharenko, L., Nicolls, M. J., Maute, A., Coster, A., & Paxton, L. J. (2012). Ionospheric and thermospheric variations associated with prompt penetration electric fields. *Journal of Geophysical Research*, *117*, A08312. https://doi.org/10.1029/2012JA017769

Moen, J., Qiu, X. C., Carlson, H. C., Fujii, R., & McCrea, I. W. (2008). On the diurnal variability in F2-region plasma density above the EISCAT Svalbard radar. *Annales de Geophysique*, *26*, 2427–2433. https://doi.org/10.5194/angeo-26-2427-2008

Oksavik, K., Ruohoniemi, J. M., Greenwald, R. A., Baker, J. B. H., Moen, J., Carlson, H. C., et al. (2006). Observations of isolated polar cap patches by the European Incoherent Scatter (EISCAT) Svalbard and Super Dual Auroral Radar Network (SuperDARN) Finland radars. *Journal of Geophysical Research*, *111*, A05310. https://doi.org/10.1029/2005JA011400

Ren, J., Zou, S., Gillies, R. G., Donovan, E., & Varney, R. H. (2018). Statistical characteristics of polar cap patches observed by RISR-C. *Journal of Geophysical Research: Space Physics*, *123*, 6981–6995. https://doi.org/10.1029/2018JA025621

Rideout, W., & Coster, A. (2006). Automated GPS processing for global total electron content data. *GPS Solutions*, *10*(3), 219–228. https://doi.org/10.1007/s10291-006-0029-5

Rodger, A. S., Pinnock, M., Dudeney, J. R., Baker, K. B., & Greenwald, R. A. (1994). A new mechanism for polar patch formation. *Journal of Geophysical Research*, *99*(A4), 6425–6436. https://doi.org/10.1029/93JA01501

Ruohoniemi, J. M., & Baker, K. B. (1998). Large-scale imaging of high-latitude convection with Super Dual Auroral Radar Network HF radar observations. *Journal of Geophysical Research*, *103*(A9), 20,797–20,811. https://doi.org/10.1029/98JA01288

Sato, T., & Rourke, G. F. (1964). F-region enhancements in the Antarctic. *Journal of Geophysical Research*, *69*(21), 4591–4607. https://doi.org/10.1029/jz069i021p04591

Shepherd, S. G. (2014). Altitude-adjusted corrected geomagnetic coordinates: Definition and functional approximations. *Journal of Geophysical Research: Space Physics*, *119*, 7501–7521. https://doi.org/10.1002/2014JA020264

St.-Maurice, J.-P., & Torr, D. G. (1978). Nonthermal rate coefficients in the ionosphere: The reactions of O^+ with N_2, O_2, and NO. *Journal of Geophysical Research*, *83*(A3), 969–977. https://doi.org/10.1029/JA083iA03p00969

Thomas, E. G., Baker, J. B. H., Ruohoniemi, J. M., Clausen, L. B. N., Coster, A. J., Foster, J. C., & Erickson, P. J. (2013). Direct observations of the role of convection electric field in the formation of a polar tongue of ionization from storm enhanced density. *Journal of Geophysical Research: Space Physics*, *118*, 1180–1189. https://doi.org/10.1002/jgra.50116

Tsunoda, R. T. (1988). High-latitude F region irregularities: A review and synthesis. *Reviews of Geophysics*, *26*(4), 719–760. https://doi.org/10.1029/RG026i004p00719

Valladares, C. E., Basu, S., Buchau, J., & Friis-Christensen, E. (1994). Experimental evidence for the formation and entry of patches into the polar cap. *Radio Science*, *29*(1), 167–194. https://doi.org/10.1029/93RS01579

Valladares, C. E., Decker, D. T., Sheehan, R., & Anderson, D. N. (1996). Modeling the formation of polar cap patches using large plasma flows. *Radio Science*, *31*(3), 573–593. https://doi.org/10.1029/96RS00481

Vierinen, J., Coster, A. J., Rideout, W. C., Erickson, P. J., & Norberg, J. (2016). Statistical framework for estimating GNSS bias. *Atmospheric Measurement Techniques*, *9*, 1303–1312. https://doi.org/10.5194/amt-9-1303-2016

Walker, I. K., Moen, J., Kersley, L., & Lorentzen, D. A. (1999). On the possible role of cusp/cleft precipitation in the formation of polar-cap patches. *Annales Geophysicae*, *17*(10), 1298–1305. https://doi.org/10.1007/s00585-999-1298-4

Wang, Z., Zou, S., Coppeans, T., Ren, J., Ridley, A., & Gombosi, T. (2019). Segmentation of SED by boundary flows associated with westward drifting partial ring current. *Geophysical Research Letters*, *46*, 7920–7928. https://doi.org/10.1029/2019GL084041

Waters, C. L., Anderson, B. J., & Liou, K. (2001). Estimation of global field aligned currents using the Iridium® system magnetometer data. *Geophysical Research Letters*, *28*(11), 2165–2168. https://doi.org/10.1029/2000GL012725

Weber, E. J., Buchau, J., Moore, J. G., Sharber, J. R., Livingston, R. C., Winningham, J. D., & Reinisch, B. W. (1984). F layer ionization patches in the polar cap. *Journal of Geophysical Research*, *89*(A3), 1683–1694. https://doi.org/10.1029/JA089iA03p01683

Zhang, Q. H., Lockwood, M., Foster, J. C., Zhang, S. R., Zhang, B. C., McCrea, I. W., et al. (2015). Direct observations of the full Dungey convection cycle in the polar ionosphere for southward interplanetary magnetic field conditions. *Journal of Geophysical Research: Space Physics*, *120*(6), 4519–4530. https://doi.org/10.1002/2015JA021172

Zou, S., Moldwin, M. B., Ridley, A. J., Nicolls, M. J., Coster, A. J., Thomas, E. G., & Ruohoniemi, J. M. (2014). On the generation/decay of the storm-enhanced density plumes: Role of the convection flow and field-aligned ion flow. *Journal of Geophysical Research: Space Physics*, *119*, 8543–8559. https://doi.org/10.1002/2014JA020408

Zou, S., & Ridley, A. J. (2016). Modeling of the evolution of storm-enhanced density (SED) plume during the Oct. 24–25, 2011 geomagnetic storm. In C. R. Chappell, R. W. Schunk, P. M. Banks, J. L. Burch, & R. M. Thorne (Eds.), *Magnetosphere-ionosphere coupling in the solar system*, *Geophysical Monograph Series* (Vol. 222, pp. 205–213). Hoboken, NJ, USA: John Wiley & Sons, Inc. https://doi.org/10.1002/9781119066880.ch16

Zou, S., Ridley, A. J., Moldwin, M. B., Nicolls, M. J., Coster, A. J., Thomas, E. G., & Ruohoniemi, J. M. (2013). Multi-instrument observations of SED during 24–25 October 2011 storm: Implications for SED formation processes. *Journal of Geophysical Research: Space Physics*, *118*, 7798–7809. https://doi.org/10.1002/2013JA018860